EUV-induced plasma: a peculiar phenomenon of a modern lithographic technology

Please check the document version of this publication:

• A submitted manuscript is the version of the article upon submission and before peer-review. There can be important differences between the submitted version and the official published version of record. People interested in the research are advised to contact the author for the final version of the publication, or visit the DOI to the publisher's website.
• The final author version and the galley proof are versions of the publication after peer review.
• The final published version features the final layout of the paper including the volume, issue and page numbers.

Link to publication

Review

EUV-Induced Plasma: A Peculiar Phenomenon of a Modern Lithographic Technology

Job Beckers [1],* , Tijn van de Ven [2] , Ruud van der Horst [2], Dmitry Astakhov [3],† and Vadim Banine [1,2]

[1] Department of Applied Physics, Eindhoven University of Technology, P.O. Box 513, 5600MB Eindhoven, The Netherlands
[2] ASML The Netherlands B.V., P.O. Box 324, 5500AH Veldhoven, The Netherlands
[3] Institute for Spectroscopy of the Russian Academy of Sciences, Fizicheskaya str. 5, Troitsk, Moscow 108840, Russia
* Correspondence: j.beckers@tue.nl; Tel.: +31-40-247-4043
† ISTEQ B.V., High Tech Campus 9, 5656 AE Eindhoven, The Netherlands.

check for updates

Featured Application: This work finds application in Extreme Ultraviolet (EUV) lithography in general. More specifically, the results may impact the development of EUV optical components used in the related equipment.

Abstract: After a long period of relatively low interest, science related to effects in the Extreme Ultraviolet (EUV) spectrum range experienced an explosive boom of publications in the last decades. A new application of EUV in lithography was the reason for such a growth. Naturally, an intensive development in such area produces a snowball effect of relatively uncharted phenomena. EUV-induced plasma is one of those. While being produced in the volume of a rarefied gas, it has a direct impact onto optical surfaces and construction materials of lithography machines, and thus has not only scientific peculiarity, but it is also of major interest for the technological application. The current article provides an overview of the existing knowledge regarding EUV-induced plasma characteristics. It describes common, as well as distinguishing, features of it in comparison with other plasmas and discusses its interaction with solid materials. This article will also identify the gaps in the existing knowledge and it will propose ways to bridge them.

Keywords: Extreme Ultraviolet; lithography; EUV; EUV-induced plasma; photon-induced plasma; MCRS; Electron density; Ion energy distribution function; IEDF; EUVL

1. Introduction

EUV-Induced Plasma and Its Relation to Photolithography

Photolithography is one of the key steps in the production process of semiconductor structures, i.e., computer chips, on the nanoscale. In these systems, a pattern on a so-called reticle is imaged in a repetitive way on each single microchip by an optical system, which decreases the image on a spatial scale by a factor of 4. To the end of fulfilling the ever-lasting drive for shrinking the dimensions of the features on such chips, the following two well-known equations for the system's resolution or critical dimension (CD):

$$CD = \frac{k_1 \lambda}{NA} \tag{1}$$

and the depth of focus (DOF)

$$DOF = \pm\frac{k_2\lambda}{(NA)^2} \qquad\qquad (2)$$

are crucial [1]. In these equations, k_1 and k_2 are process dependent constants, λ is the wavelength of the light used, and $NA = n\sin\alpha$ is the numerical aperture of the used lens with n and α the refractive index of the medium surrounding the lens and the acceptance angle of the lens, respectively. Decreasing the feature size on a chip requires increasing NA and/or conducting the photolithographic process at a smaller wavelength. In the past, the wavelength of the light used has been scaled down from 436 nm (g-line) to 365 nm (i-line) to 248 nm (KrF) to 193 nm (ArF). The most advanced deep Ultraviolet (DUV) machines that are currently in the field employ "immersion lithography"—introduced in 1987 [2]—where the lens is immersed in a medium with a higher refractive index (e.g., in water with $n = 1.43$). This has led to an increase of NA up to 1.35. The shift from the 22 nm to the 14 nm node was achieved with double patterning lithography based on 193 nm DUV systems [3].

Photolithography using Extreme Ultraviolet (EUV) photons with wavelengths of 13.5 nm (and energies of 92 eV) has been introduced with the eye on achieving significant cost reduction (per produced chip) and downscaling of the feature size even more [4]. Several types of EUV sources have been, or are, under development for the production of the high flux of needed EUV photons. Besides the relatively low power xenon-based EUV sources [5], types of high power EUV sources include EUV sources that are based on laser produced plasmas (LPP) from tin droplets [6–8] and EUV sources that are based on laser-assisted discharge produced plasmas (DPP) in tin vapor [9].

Lithography tools ideally operate under vacuum conditions since EUV photons are effectively absorbed by almost any medium. However, for technical reasons, modern lithographic tools using EUV light operate in 1–10 Pa hydrogen background gas [3].

Inherently, everywhere, such photons travel through the background gas, neutral gas particles are photo-ionized, and plasma is created. These so-called EUV-induced plasmas are highly transient in time and they initially contain highly energetic electrons (76 eV) that thermalize on time scales of 100 ns—10 μm, depending on the system's conditions. Especially, in the early stages of the afterglow of such pulsed plasma, the highly energetic electrons may create additional plasma species due to consecutive electron impact ionization of gas neutrals, while ionic compounds are accelerated towards plasma-facing surfaces—EUV-induced plasmas interact with the machine by means of, for instance, initiating plasma-enhanced chemistry, ion bombardment of delicate plasma-exposed surfaces, and enabling contamination transport to positions in the machine where harm is most dominantly felt. It is not only to fulfill scientific curiosity with respect to this peculiar type of plasma, but also for its practical implications towards EUV lithography (EUVL) that research groups all over the world have started considerable research efforts.

The current article provides an overview of the existing knowledge regarding EUV-induced plasma characteristics, describes common as well as distinguishing features of such plasmas in comparison with other plasmas, and discusses its physical interaction with solid materials. This paper will also identify the gaps in the existing knowledge and will propose ways to bridge them.

This article is organized, as follows. Section 2 will focus on the bulk properties and the dynamics of EUV-induced plasmas, while Section 3 will elaborate on the mechanisms and implications of this plasma when contacting surfaces, such as EUV optical components. Finally, Section 4 identifies the upcoming research areas and proposes new research efforts to bridge knowledge gaps and to answer the most urgent questions.

2. EUV-Induced Plasma

2.1. Observation of a Peculiar Phenomenon: EUV-Induced Plasma

In 2006, researchers at the research department of world leader in photolithography systems ASML reported a peculiar phenomenon that would later be referred to as "EUV-induced plasma" [10]. A glow was created upon sending a pulsed beam of EUV photons through a low pressure (a few

Pa) background gas (see Figure 1). Even by the naked eye, it could be observed that the created plasma—or more specifically the excited plasma species that radiate in the visible spectrum—was visually confined in space. Although the state of this matter (plasma) and its potential impact on the lithography tool was immediately recognized, the relevant mechanisms where far from understood and key parameters of this plasma where not known at all. As a reaction, several research groups around the world started to perform both experimental and numerical studies with the aim of unraveling this plasma's secrets. In this part, we elaborate first on the key parameters to be expected in EUV-induced plasmas in Section 2.2. With these parameters in mind, Sections 2.3 and 2.4, respectively, review the governing numerical and experimental research efforts that have been undertaken until today. Section 2.5 describes the principle mechanisms behind the plasma formation and subsequent plasma dynamics, while Section 2.6 summarizes the relevant scaling laws with respect to the plasma densities to be expected under scanner conditions. It should be noted that—although measurements have been conducted in other gases, such as argon as well [11]—only EUV-induced plasmas in H_2 background gas are discussed in detail in this work. The reason for this is that today's lithographic tools are operated while using low pressure H_2 gas [3].

Figure 1. Photograph of the inner side of an experiment chamber in which a low pressure (argon) gas is irradiated with a pulsed beam of Extreme Ultraviolet (EUV) photons. The blueish glow at the position where the EUV beam travels indicates the interaction between the EUV photons and the gas.

2.2. Key Parameters of EUV-Induced Plasma

As can be observed in Figure 1, plasma is created everywhere that the pulsed EUV light travels through and interacts with the background gas. The EUV photon flux decreases, while the beam travels through the tool, due to the absorption of these photons. The absorbed time-dependent intensity $I_{abs}(t)$ of the EUV light is governed by:

$$I_{abs}(t) \;=\; I_0(t)\Big[1 - exp\big[-n_{gas}\sigma_{pi}l_{abs}\big]\Big] \approx I_0(t)n_{gas}\sigma_{pi}l_{abs} \tag{3}$$

Here, $I_0(t)$ is the initial intensity of the EUV pulse, n_{gas} is the initial neutral gas density, σ_{pi} is the total photoionization cross section, and l_{abs} is the length of the light path under investigation. Of course, σ_{pi} depends on the type of gas and on the wavelength of the light used. In the current generation EUV scanners, a budget of 4% of transmission is reserved for losses due to absorption by gas molecules (from the intermediate focus (IF)—i.e., the interface between EUV source and scanner—to the wafer) [3]. This loss is directly related to the creation of plasma species through direct photoionization events creating fast electrons (i.e., ~77 eV in H_2). Secondary electron emission from EUV-irradiated surfaces is another possible source of energetic electrons. On their turn, these fast electrons may produce additional plasma species through electron-impact ionization events, and further lose energy through other inelastic processes (e.g., various excitations of H_2 molecules).

Where ion fluxes, ion energy distributions functions (IEDFs), and radicals describe to a large extent the interaction of plasma with plasma-facing surfaces (subject of Section 3), two quantities that

are predominantly important in describing the "ecosystem" in the bulk of the pulsed plasma are the density and the temperature of the free electrons. Note that, although negative H^- ions may be formed as well in hydrogen plasmas, it was derived by Astakhov et al. [12]—while using cross sections for dissociative electron attachment of highly vibrationally excited H_2^* (e.g., $\upsilon = 4$) [13] and for direct excitation to such states [14]—that the densities of H^- ions are negligible in the current case.

2.2.1. Electron Density

When considering Equation (3), one would expect an initial plasma density—primary due to photo-ionization by EUV photons—that varies over several orders of magnitude, depending on the local gas pressure, EUV power, EUV beam waist, and gas type. The highest plasma density can most likely be found in the foci, where the EUV light has the highest flux. Most of the laboratory experiments have utilized a xenon-based discharge produced plasma (DPP) source, operating at a typical frequency of 500 Hz, as a source of EUV radiation. For reference, typical laser produced plasma (LPP) sources in the field use repetition rates that are two orders higher, i.e., up to 50 kHz [7,15]. Of course, as time after the EUV pulse passes, the plasma density may further increase due to consecutive electron impact ionization (dependent on the background gas pressure), followed by a decrease due to plasma expansion in the free space. Finally, plasma termination occurs at a surface in the vicinity of the plasma (typically on ms time scales for cylindrical measurement volumes of 10 cm in height and 10 cm in radius [16]). Which of these processes is dominant depends on local conditions and the considered time scales. Overall, measurements of the plasma density—while using low power EUV sources—have demonstrated values up to 10^{17} m^{-3} [17].

2.2.2. Electron Temperature

The temperature of the plasma species is another important parameter when describing bulk plasmas. The temperature of neutral species may be assumed to be close to room temperature under circumstances that occur in EUV-induced plasmas for lithography applications. However, electrons have a much higher average energy than they would have at room temperature. Immediately after the first ionization events, the average electron energy equals 76.6 eV, i.e., the difference between the energy of the photons used (92 eV), and the ionization energy (15.4 eV for H_2). Most of the excess energy of the photoionization reactions is transferred to the electrons, since these have a much lower mass when compared to that of the ions and neutrals. Note that, under normal conditions, multilayer (MLM) mirrors and optical filters that are used in the system narrow down the spectrum of the source's EUV radiation closely around 13.5 nm. Therefore, the electron energy distribution function (EEDF) is highly non-Maxwellian just after the gas is irradiated. Typically, these electrons thermalize—again dependent on the experimental conditions—on time scales in the order of 1–100 µs [18]. Figure 2 shows computer simulations of the EEDF for an EUV-induced plasma at four different moments in time after the start of the EUV pulse. Here, the dashed lines—that represent Maxwellian EEDF's—indicate that at the time the EUV intensity is highest, i.e., 0.04 µs after the start of the pulse, the EEDF is far from Maxwellian shaped. When irradiation by EUV photons has vanished, i.e., 0.3 µs after the start of the pulse, electrons already significantly cooled down, and—even more importantly—their EEDF has become close to Maxwellian-shaped.

Finally, the initially produced ions have thermal energies that are close to room temperature. However, in the vicinity of solid surfaces, the plasma self-induces a space charge region—in traditional plasmas often named a plasma sheath—that creates a potential difference between the bulk plasma and the facing surface. Section 3 discusses the anisotropic acceleration of (positive) ions by the created electric field present in this space charge region and the diagnostics. Some ionic species, such as H^+, show an energetic tail in their energy distribution function that can be correlated to their formation mechanism. Section 3 will also further discuss this.
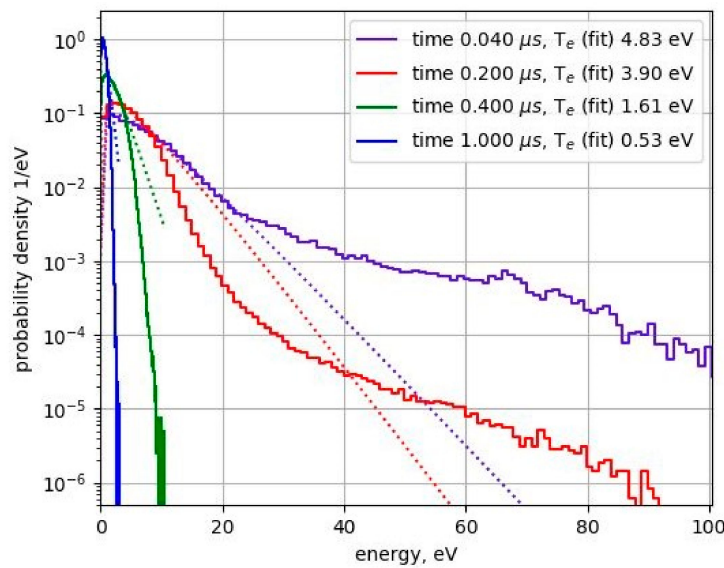
Figure 2. Particle-in-cell simulated electron energy distribution functions (EEDFs) in an EUV-induced plasma during the EUV pulse (purple curve, at $t = 0.04$ μs the EUV intensity has its maximum value), at the end of the EUV pulse (red curve) and at different moments in time after the EUV pulse ($t = 0.4$ μs and $t = 1$ μs are approximately 0.2 μs and 0.8 μs after the end of the EUV pulse, respectively). The colored dashed-lines represent Maxwellian EEDFs with a temperature corresponding to the calculated mean electron energy.

2.3. Recent Numerical Work on EUV-Induced Bulk Plasmas

The usual choices for modelling of EUV-induced plasmas are kinetic methods from the particle-in-cell (PIC) family [19]. The PIC method allows for accommodating an arbitrary shape of the energy distribution function against reasonable computational costs. To the authors' knowledge, the first PIC modelling of EUV-induced plasmas was performed by Wieggers, Goedheer and Louis [20]. These authors used one-dimensional (1D) particle-in-cell codes and estimated the damage to a multilayer mirror (MLM) due to physical sputtering. The comparison between numerical outputs and experiments, and validation was limited due to the 1D nature of the codes and the non-1D geometry of experimental systems.

The next steps included the development of an EUV-induced plasma tailored two-dimensional particle-in-cell code, which several experiments validated [21,22]. These efforts enabled modeling plasmas induced by irradiation with one single pulse of EUV radiation. It was found that an accurate set of differential cross-sections was needed for the description of the ignition of such an EUV-induced plasma, since the models' results were very sensitive to the energy distribution between the two electrons that were produced after ionization [21]. This conclusion correlates with the work of Mokrov and Riser [23], who found as well that differential cross-sections were crucial for an accurate description of ionization coefficients.

Although single pulse modelling matches reasonably well with experiments (see Figure 3) [21], these models were not sufficiently developed to accurately describe the full situation under scanner conditions. This is because, typically, tin-based LPP sources in the field use repetition rates up to 50 kHz [7,15]. According to these modeling efforts, the electron temperature in an EUV-induced plasma in low pressure H_2 gas decreases to 0.1 eV within a few μs after plasma initiation. Hence, for the enclosing chamber with characteristic dimensions mentioned before, the accumulation of plasma would occur at increased repetition rates. However, it is hardly possible to describe this situation with solely a PIC approach due to the very large simulation time that is needed.
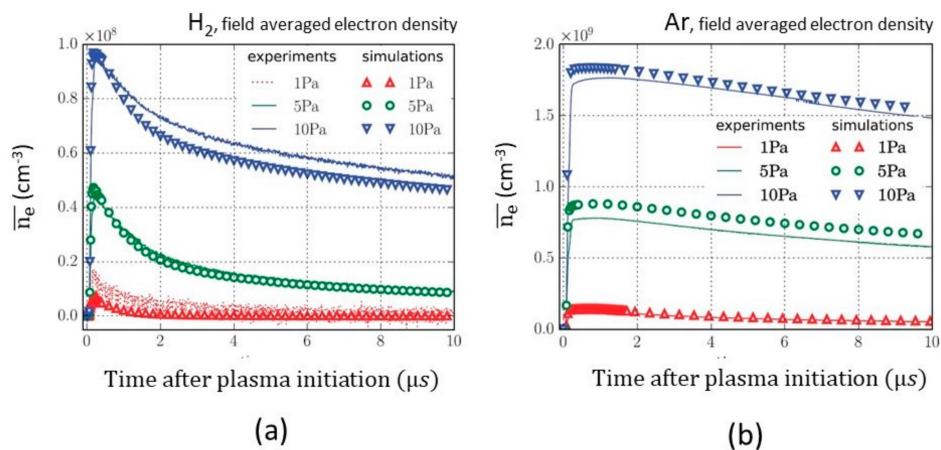
Figure 3. Examples of numerical PIC simulations matching reasonably well measurement of the electron density (measured with Microwave Cavity Resonance Spectroscopy, see next section) in EUV-induced plasmas after irradiation of low pressure hydrogen (**a**) and argon (**b**) gas by one single pulse of EUV radiation. Figure produced using data from [21].

To that end, an attempt was recently made to estimate the accumulation effects via auxiliary diffusion simulations, in which all the complex effects are summed to an effective source term that was computed by a PIC code. The effects of EUV-induced plasma ignition in pre-existing plasmas were estimated by additional PIC simulations. This approach has shown reasonable agreement with experiments in the cases where plasma accumulation is large (e.g., >100 pulses are accumulated) [24]. Nevertheless, a better solution is needed, especially when simulating accumulation over fewer pulses (e.g., <10 pulses), since the injection of electrons into the plasma can increase fluxes of plasma-created species to the walls [25].

2.4. Recent Experimental Work on EUV-Induced Bulk Plasmas

One of the most obvious ways to study light-emitting plasmas is by making photographs of it. This task is best performed using intensified charge-coupled device (iCCD) cameras, since the relevant time scales are short (ns-µs) and light emission levels are low. Figure 4 shows iCCD photographs visualizing the region where the EUV-induced plasma emits light in the UV and visible spectrum, together with time-resolved measurements of the total and wavelength-integrated intensity and the EUV-irradiation intensity.
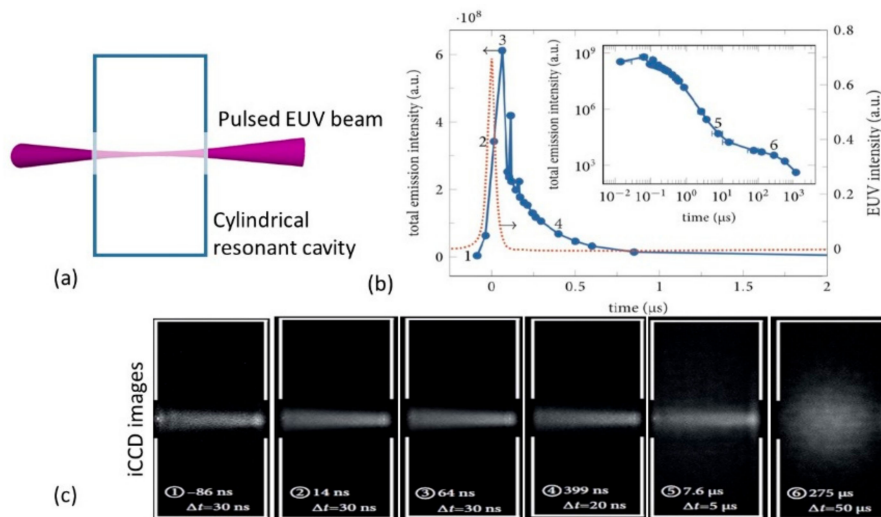
Figure 4. (**b**) Total emission (in the UV and visible spectrum range) from an EUV-induced plasma in 5 Pa argon created inside a cylindrical measurement volume (**a**). The numbers displayed in this figure correspond to the numbered images in (**c**). The horizontal error bars represent the set intensified charge-coupled device (iCCD) camera's gate width. (**c**) Gated iCCD images at various moments in time (indicated in each picture individually) after one pulse of EUV-irradiation. The beam of EUV photons is directed through a cylindrical aluminum measurement chamber from the left to the right (the side walls are indicated with white lines). The side walls of the measurement chamber are made of a mesh for visibility and the top and bottom lids contain concentric holes for entrance and exit of the EUV beam. Δt indicates the used gate width of the camera. Intensities are normalized for each image individually. Figure produced using data from [26].

Fundamental processes in EUV-induced plasmas have been investigated by cleverly using the fact that EUV-induced plasmas radiate in the EUV and UV/visible range. At considerably higher pressures (close to atmospheric pressure) than expected in EUV lithography tools (a few Pa), Bartnik et al. [27–30] used spectral measurements to study ionic states in EUV-induced plasmas in various gases, such as xenon, argon, neon, and helium. In photoionized plasmas in argon, they used laser interferometry to measure electron densities up to 10^{24} m^{-3}. Saber et al. [31] used spectroscopic measurements in the ultraviolet/visible range to obtain local information regarding the temperature and density of electrons in EUV-induced plasmas in a mixture of Kr/Ne/H$_2$ gas. Values of 0.9 to 1.7 eV and 10^{21} to 10^{22} m^{-3} were found for the temperature and density of electrons in that research, respectively. Although these investigations provide valuable information with respect to understanding the fundamental behavior of photoionized gases, we remain close to the pressure range used in EUVL in the following of this manuscript (i.e., 1–10 Pa).

As mentioned before, plasma bulk dynamics are most dominantly described by the temperature (T_e) and density (n_e) of free electrons in this pressure range. From an experimental point of view, classical plasma diagnostics provide several ways to probe the presence of electrons. For instance, Thomson scattering [32]—based on the scattering of laser light by free electrons—enables the retrieval information about the energy and density of free electrons in plasma. However, this technique only delivers sufficient signal at electron densities of 10^{17} m^{-3} and higher [32], meaning that this technique is not suitable to probe electrons in EUV-induced plasmas under scanner-like conditions. Another technique that is commonly used for this purpose includes the utilization of traditional Langmuir probes from which the voltage-current characteristics provide information regarding n_e and T_e. Although this technique may be able to probe electrons in the here relevant density range, Van de Velden et al. [33] concluded that it was not feasible to apply probes to EUV-induced plasmas, with the main reason being that the photo-electric currents obscured the measurements of the I-V curves. Later,

Astakhov et al. came to a similar conclusion by experimental work that was analyzed while using different probe theories and compared to numerical simulations [12,22].

From 2015 onwards, Microwave Cavity Resonance Spectroscopy (MCRS) has been applied and further developed as non-intrusive, accurate diagnostic to investigate the creation, dynamics, and decay of highly transient pulsed plasma environments under EUVL scanner conditions [11,17,18,21,26,34,35]. The diagnostic has provided experimental data to interpret plasma physical processes on the most fundamental level [16,36] and to verify numerical models since its introduction [17,21]. The basic principles behind MCRS are briefly summarized in the following of this section. The reader is referred to the literature referenced above for more details.

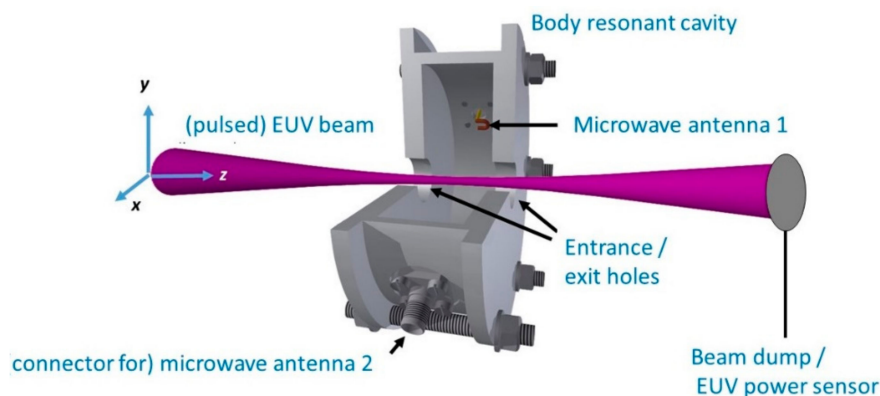Microwave Cavity Resonance Spectroscopy (MCRS)

Brown and Rose first proposed the utilization of the interaction between microwaves and plasma to probe electrons [37–39]. Later, this principle has been used in many studies, for instance to the end of measuring the density of free electrons in low pressure radiofrequency driven gas discharges [40]. In concert with laser-induced photodetachment, MCRS has even appeared as a feasible diagnostic to measure the density of negative ions in for instance etching [41–43] and in powder forming plasmas [44–48]. Recently, MCRS has even been applied as an electron diagnostic in plasmas at atmospheric pressure [49].

In MCRS-based diagnostics, the plasma under study is enclosed by a (cylindrical) resonant cavity. By sending in low power microwave radiation—for instance by means of an antenna through one of the side walls—a resonant mode might be excited at certain frequencies. These resonant frequencies are determined by I) the geometry of the plasma enclosing cavity (which is ideally fixed during experiment) and II) the permittivity ε of the medium inside the cavity volume. It is the change of ε due to the presence of free electrons in the cavity volume that is key to this diagnostic. Hence, by measuring the difference $\Delta\omega = \omega - \omega_0$ between the resonant frequency ω of a plasma-filled cavity and the resonant frequency ω_0 of an empty cavity, the density n_e of free electrons can be computed from [11]:

$$\overline{n_e} = \frac{2m_e\varepsilon_0\omega^2}{e^2}\frac{\Delta\omega}{\omega_0} \tag{4}$$

where e and m_e are the charge and mass of an electron, respectively, and ε_0 is the permittivity of vacuum.

In practice, MCRS has been applied to EUV-induced plasmas by sending a pulsed EUV beam through a cavity that contained holes in its top and bottom cavity lids for this purpose (see Figure 5) [11,17,18,34,35,50]. Microwave (MW) antennas that are inserted through the cavity wall are used to send in microwave radiation and to record the cavity's response (either in transmission or reflection mode). More experimental details can be found in the above referenced literature.


Figure 5. Microwave Cavity Resonance Spectroscopy (MCRS) configuration for probing free electrons in an EUV-induced plasma. The pulsed beam of EUV light is directed through a resonant cavity.

It should be noted that the bar on $\overline{n_e}$ in Equation (4) indicates that this value is cavity-volume averaged and is weighted with the squared electric field distribution $E^2(\vec{r})$ of the resonant mode inside the cavity:

$$\overline{n_e} \; = \; \frac{\iiint n_e(\vec{r})E^2(\vec{r})d^3\vec{r}}{\iiint E^2(\vec{r})d^3\vec{r}} \tag{5}$$

This means that electrons that were present in the cavity volume are probed to the highest extent at positions, where the used resonant mode has its maximum field strength (e.g., on the cavity's axis when the TM_{010} mode (see Figure 6a) is used and roughly at half the cavity's radius when the TM_{110} mode (see Figure 6b) is used).
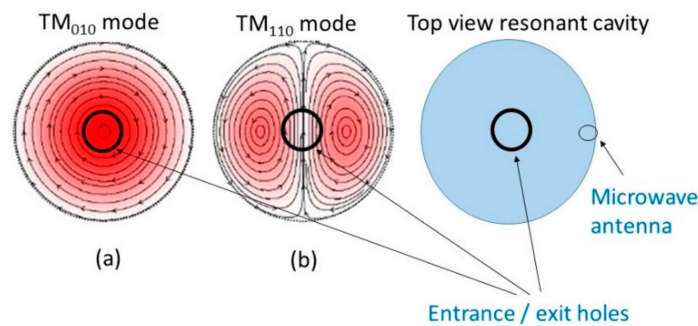
Figure 6. Top view of the electric field distributions of two resonant modes (TM_{010} (**a**) and TM_{110} (**b**)) inside a resonant cavity demonstrating the different local sensitivities. Figure produced using data from [51].

Despite the fact that MCRS is a strong diagnostic that has delivered valuable information and understanding regarding EUV-induced plasmas, its volume-averaged nature has always been considered to be disadvantageous, since local plasma physical effects could—in this configuration—not be resolved. However, recent developments have led to the introduction of multi-mode MCRS being able to resolve electron density profiles, not only temporally (~100 ns time resolution), but also spatially resolved (~100 μm spatial resolution) with a lower detection limit as low as $n_e = 10^{12}$ m^{-3} [51]. This has been previously used to spatially resolve the center point and the cross-sectional intensity profile of a pulsed EUV beam (see a typical example in Figure 7) [52].
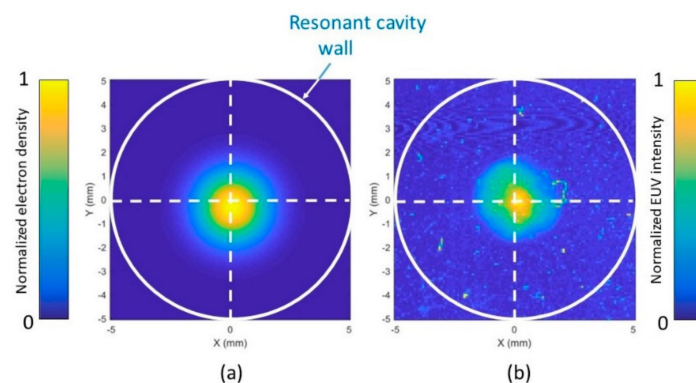
Figure 7. (**a**) Initial electron density profile—retrieved from multi-mode MCRS measurements—induced by irradiation of a low pressure gas by pulsed EUV radiation (at the maximum intensity of in-band EUV emission from a xenon-based discharge produced plasmas EUV (DPP EUV) source) and (**b**) an independent measurement of the beam intensity profile at the position of the cavity. False colors are plotted on a linear scale and normalized. Figure produced using data from [51].

2.5. Dynamics of EUV-Induced Plasmas

Figure 8 depicts the typical evolution of the density $\overline{n}_e$ of free electrons in a resonant cavity that was obtained from MCRS measurements before, during, and after a low pressure (1–10 Pa) H$_2$ gas was irradiated with a pulse of EUV radiation [17]. $\overline{n}_e$ is locally weighted with the square of the (microwave) electric field and volume averaged. $\overline{n}_e$ is plotted in normalized values, since absolute values strongly vary with experimental parameters, such as gas pressure, pulse energy, and gas type. Absolute values that are below 10^{17} m^{-3} are typical densities expected for these kinds of plasma. Phenomenologically, the basic plasma processes can be split up into three different consecutive phases in time (see Figure 8). In Phase I, $\overline{n}_e$ strongly increases upon irradiating the gas with EUV photons. In Phase II, there is no EUV-irradiation and $\overline{n}_e$ decreases at a rate that is faster than exponential. In the last phase—Phase III—an exponential decay rate of the plasma sets in. Below, Phases I-III will briefly be discussed in consecutive order.
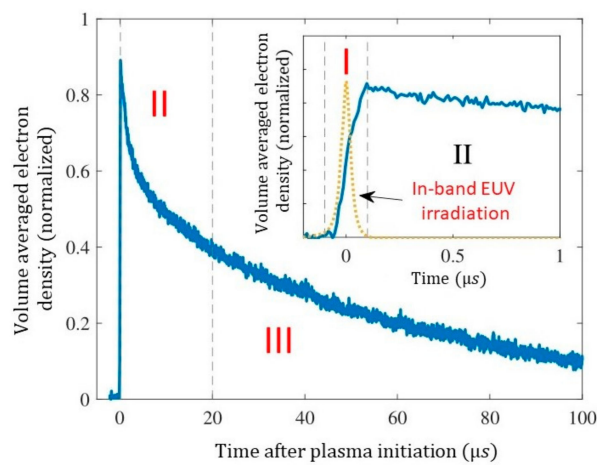
Figure 8. Typical electron density $\overline{n}_e$ in an EUV-induced plasma in H$_2$ averaged over the measurement geometry. The figure inset is a zoom in up to 1 μs along with the temporally resolved EUV intensity with which the gas is irradiated. The consecutively occurring phases I, II, and III are discussed in the text below. Figure produced using data from [24].

2.5.1. Phase I: Plasma Creation by Photoionization and Electron Impact Ionization

Photoionization

From Figure 8 it can be observed that, free electrons are created in Phase I, upon EUV-irradiation of the H$_2$ background gas. The three dominant photon-induced processes are single photoionization (Equation (6)), dissociative photoionization (Equation (7)), and double photoionization (Equation (8)).

$$H_2 + h\nu \rightarrow e + H_2^+ \tag{6}$$

$$H_2 + h\nu \rightarrow e + H_2^{+*} \rightarrow e + H^{(*)} + H^+ \tag{7}$$

$$H_2 + h\nu \rightarrow 2e + H_2^{2+} \rightarrow 2e + 2H^+ \tag{8}$$
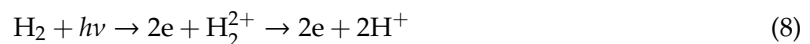
The cross sections for the reactions in Equations (6)–(8) are given in Figure 9 as a function of the photon energy in the range 20–120 eV. At photon energies of 92 eV (i.e., 13.5 nm), which is relevant for EUVL, contributions from single photoionization (roughly 80%) mainly dominate the total photoionization cross section $\sigma_{pi} = 6.5 \times 10^{-24}$ m^2.
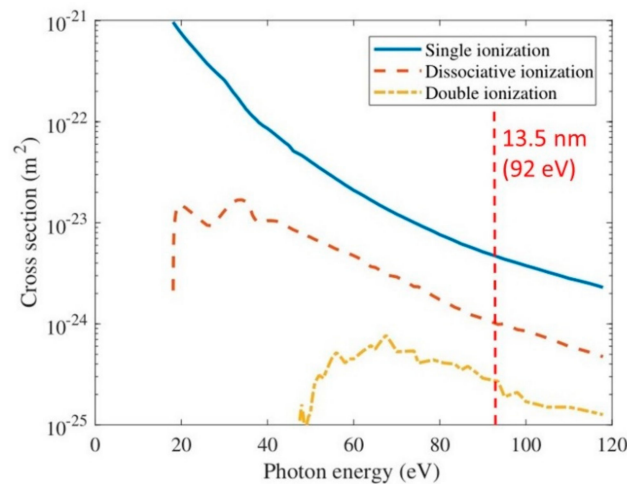
Figure 9. Cross sections for single, dissociative and double photoionization of molecular hydrogen as a function of the photon energy. Figure produced using data from [16,53–55].

In general, the photon energy in lithography systems considerably exceeds the ionization energy of the used gas; e.g., 15.4 eV for the transition from the ground state of hydrogen (H_2, $X^1\Sigma_g^+$) to the stable ionic ground state (H_2^+, $1s\sigma_s$). This excess energy is mainly transferred to the ejected electron, which then has an energy of 76.6 eV, while the created H_2^+ ion remains relatively 'cold' at room temperature.

Equation (7) shows that H^+ ions are created through dissociation of an electronically excited H_2^{+*} state with an atomic H radical as a second reaction product. The excess energy of this reaction is evenly distributed over the ionic and radical compounds since the ion and radical have similar masses (each about 8 eV [56]).
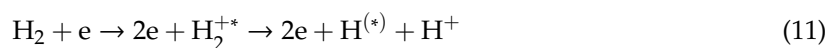
The same principle accounts for Equation (8), where H_2^{2+} is highly unstable by definition. Upon dissociation of this compound, 18.8 eV is evenly distributed over the two resulting H^+ ions [57]. Overall, due to photoionization events, during EUV-irradiation, initial plasma is created that also contains H^+ and H_2^+ and radicals, besides electrons (both fast and slow). Additionally, on small time scales (~200 ns) H_2^+ and H_2 may react as [58]:

$$H_2^+ + H_2 \rightarrow H_3^+ + H \tag{9}$$

to form H_3^+ ions. Whereas, H_3^+ has been recognized as the dominant ion in radiation-induced plasmas in H_2 background gas in outer-space, recent research has shown that this ion is also dominant under lithography scanner conditions on time scales longer than a few 100 ns after irradiation [59].

Electron Impact Ionization

As mentioned earlier, the free electrons have an energy up to 76.6 eV after the first ionization events have occurred, depending of the production process. Upon collision, these electrons may ionize the H_2 background gas even further by electron impact ionization. Comparable to photoionization (Equations (6)–(8)), the three electron impact ionization processes playing a role in hydrogen are single ionization (see Equation (10)), dissociative ionization (see Equation (11)), and double ionization (Equation (12)).

$$H_2 + e \rightarrow 2e + H_2^+ \tag{10}$$

$$H_2 + e \rightarrow 2e + H_2^{+*} \rightarrow 2e + H^{(*)} + H^+ \tag{11}$$

$$H_2 + e \rightarrow 3e + H_2^{2+} \rightarrow 3e + 2H^+ \tag{12}$$
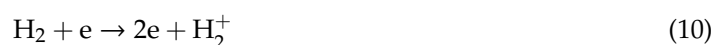
From a plasma dynamic point of view, the electrons dominate this phase, since the inertia of the much heavier ions prevents them from moving over distances that are comparable to that of the free electrons on these short time scales. The presence of a surface in contact with plasma leads to the creation of space charge regions, which are—via the Poisson equation—accompanied by strong electric fields [60]. Directly after the creation of EUV-induced plasmas (i.e., in this phase), the process towards the creation of this space charge is twofold. First, a part of the fast and highly mobile photo-electrons escape towards nearby walls [11]. The resulting charge imbalance and the associated potential well traps the remaining electrons. During this phase, the plasma potential as compared to the plasma facing surfaces can be over 50 V [21,61].

2.5.2. Phase II: Strong Decrease of $\overline{n}_e$

In Phase II, there is no irradiation of the volume with EUV photons, i.e., there is no external energy source. However, the energetic electrons that were generated in the previous phase can still contribute to ionization, for instance by means of electron-impact ionization. Furthermore, in this second phase, the plasma expands towards the walls of the measurement volume and the detected (E^2-weighted and volume-averaged) $\overline{n}_e$ decreases at a rate that is faster than exponential in time due to the loss of fast electrons and their non-Maxwellian energy distribution. Overall, the ion and electron clouds expand hand-in-hand. With an eye on the MCRS diagnostic, the free electrons dynamically redistribute over the cavity volume, and hence the spatial weighting of the electron density distribution in Equation (5) alters. The time scale on which the ions start to be dragged along with the expanding electron cloud coincides with the inverse of the ion plasma frequency ω_{pi}.

$$\omega_{pi} \;=\; \sqrt{\frac{e^2 n_i}{\epsilon_0 m_i}} \tag{13}$$

and it is typically in the order of 20–100 ns, depending on initial ion density n_i and mass m_i of the relevant ions.

During this phase, the temperature of the electrons significantly decreases due to inelastic collisions. As a result, the plasma potential and electric fields towards the cavity's walls also decrease.

2.5.3. Phase III: Exponential Decay of n_e

At the start of this phase, the plasma (including the plasma ions) has expanded, such that it fills up the whole cavity volume. At moderately high pressures (above 3 Pa [18]), the main loss mechanism of plasma species is ambipolar diffusion, followed by recombination of electrons and ions at the wall. Note that, when compared to this process, three-body recombination in the volume is negligible [11], at least for EUVL relevant pressures and parameter space. The exponential decay in Phase III can be fitted with an ambipolar diffusion model since the shape of the spatial n_e distribution remains more or less unchanged (only absolute values change) [18]. From such fit, besides n_e, also values for T_e can be retrieved. It was shown that in this phase and, at pressures above 3 Pa, the electrons have cooled down to room temperature while using EUV pulse energies of (53 ± 3) µJ [18]. In the same work, it was also shown that the electrons have left the cavity volume before ions and electrons have even gotten the chance to diffuse jointly in outwards direction for pressures lower than 3 Pa. It was observed that T_e remained larger than room temperature, for these low pressures, i.e., up to 0.1 eV for pressures down to 1 Pa.

2.6. Scaling Laws

Most of the reported experiments have been conducted in conditions that, in one way or another, deviate from the conditions that are expected in current and future EUVL tools. However, from both experiments and numerical work, the scaling laws with respect to several parameters, such as EUV spectrum, gas pressure, pulse energy, repetition rate, and gas type, can be derived and are as follows.

- Influence of EUV spectrum

The spectrum of the light that is used to irradiate the system under investigation is of utmost importance. Where during normal operation the normal-incidence multi-layer mirrors in the lithography tool inherently narrow down the spectrum to a range that closely centered around 13.5 nm, experiments have also been conducted for wider spectral ranges. For instance, it was shown by the MCRS experiments that the density of an EUV-induced plasma in 10^{-4} mbar residual background gas keeps increasing significantly, even after the main in-band EUV radiation has fully vanished in the absence of a spectral purity filter (SPF) [51]. This effect was explained by out-of-band radiation that was emitted by the EUV source later in time. The fact that the contribution of out-of-band radiation to the total emission of the EUV source is relatively low, is more than compensated by the higher total ionization cross section at lower photon energies. For instance, the total ionization cross section of 2.5×10^{-21} m^2 is almost one order higher than the value of 2.5×10^{-22} m^2 at 92 eV for N$_2$ molecules (making up ~80% of the molecules) that are just above the ionization threshold (15.6 eV) [62]. An extensive study regarding the influence of the EUV spectrum on the creation of EUV-induced plasmas in hydrogen was published in Ref. [35]. In that publication, both the used spectral purity filter (no-filter, normal SPF, and aluminum filter) and source type (Xe-based EUV source versus Sn-based EUV source) demonstrated a significant effect on the plasma formation.

- Gas pressure scaling

Within the experimental range investigated [17], it has been demonstrated that the maximum obtained density of the bulk plasma scales quadratically with the pressure of the background gas. As mentioned before, the initial electrons are created by photoionization. From Equations (6)–(8), it can be understood that this process linearly scales with the H$_2$ density, i.e., pressure. These initial electrons can subsequently ionize H$_2$ by electron impact ionization, which scales with the electron density (linearly dependent on pressure) and the gas pressure (see Equations (10)–(12)). Hence, the electron density that was caused by electron impact ionization quadratically scales with pressure. This means that the pressure dependence of the total electron density has both a linear and a quadratic term, which only holds for the maximum obtained electron density in the investigated range. The electrons that were created by photoionization are only able to cause three electron impact ionization events due to the limited amount of energy (76 eV) and the lack of electron heating mechanisms. This means that the quadratic scaling will not hold for higher pressures or long time scales, since no more additional electrons will be created after a few collisions (the electrons have cooled down too much). In this regime, the density scales linearly with pressure, since every photoionization event creates in the end (via electron impact ionization) four electrons.

- Pulse energy scaling

It has been demonstrated that the maximum reached bulk plasma density just after the gas is irradiated with EUV photons is in the order of ~10^{15} m^{-3} within the experimental range investigated [16,17,34]. This density scales linearly with pulse energy.

- Source repetition rate scaling

Most of the experiments up to now have been conducted while using an EUV source with a relatively low repetition rate of 500 Hz. However, nowadays EUV scanners operate together with LPP sources at a repetition rate of up to 50 kHz [7,15]. Upscaling the repetition rate alters EUV-induced plasma dynamics significantly, as was already demonstrated in Ref. [16]. At 500 Hz repetition rate, the plasma that was created with a certain pulse of EUV photons has fully vanished at the moment the next pulse of EUV photons is applied. Experiments using a tin-based EUV source at repetition rates of 1, 5, and 10 kHz, however, show that more background plasma remains between two consecutive pulses of irradiation, at higher repetition rates [16]. This effect will also occur at higher pressures, as

higher pressures slow down the plasma decay. In the end, the build-up of the plasma background depends on the balance between the plasma decay time (as determined by pressure and geometry) and the source repetition rate.

- Different gases

EUV-induced plasmas have been investigated in several different gases (e.g., Ar, He, H_2, residual air). Of main importance in the governing plasma dynamics are the (photo-and electron-impact) ionization cross sections, which impact the maximum plasma density, the ion mass of the specific gas, which impacts the rate of plasma expansion and decay and the possibility to excite specific molecular and/or atomic energy levels. Very recently, EUV-induced plasmas in N_2-diluted H_2 gas have been studied [63]. From that study, it was concluded that the addition of even a small amount of N_2 (in the order of 0.1%) to H_2 resulted in a significant alteration of the ionic balance of the system and a rich chemistry producing NH-containing ions.

3. Bulk Materials Facing EUV Photon Induced Plasma

Current DUV lithography tools use refractive optics (i.e., lenses) for imaging. However, imaging in EUV lithography (EUVL) tools is achieved by using multilayer Bragg reflective mirrors (MLMs) since EUV radiation would be fully absorbed by these lenses. These mirrors have forty or more bilayers of molybdenum (Mo) and silicon (Si) [3]. As extensively discussed in the previous section, the presence of a low pressure (1–10 Pa) background gas results in the creation of EUV-induced plasma that is directly adjacent to these mirrors [10,34,64]. The interaction with this plasma can have both beneficial and negative effects on the (long term) mirrors' surface conditions. In this section, we first review the observations of plasma-induced surface processes. Subsequently, the relevant particle fluxes towards plasma facing surfaces are discussed with a focus on plasmas in H_2. Finally, the studies that attempted to identify the processes that dominantly impact the surface conditions are reviewed.

3.1. Observation of Cleaning and Degradation of Exposed Surfaces

Under certain conditions Mo/Si multilayers can suffer from carbon (C) deposition or silicon oxidation, as has been shown in the multiple studies using synchrotrons and vacuum UV spectrometers [65–70]. In EUVL, carbon growth is related to the presence of a monolayer of physisorbed (from the volume) hydrocarbon molecules on all of the surfaces. These hydrocarbon molecules are partly dissociated during EUV exposure by direct photon absorption and/or secondary electrons that are emitted from the surface [65,66,71]. The radicals that are created during this process, react with the mirror's surface, which leads to a fast build-up of carbon. The relevance of this case for EUVL is due to the relative reflectance loss $\Delta R/R$ due to either carbon contamination or additional oxygen presence during oxidation.

Carbon contamination can successfully be removed by remote plasma cleaning [72] and atomic hydrogen etching [73]. Furthermore, reactive ion etching by surface-facing EUV-induced plasmas in hydrogen has also appeared to be capable of cleaning carbon contamination [64]. On the other hand, oxidation of the silicon layers is permanent. The first step in the reaction mechanism for oxidation of silicon is similar to that initiating carbon deposition, but with adsorbed water instead of hydrocarbons. Irradiation with photons, electrons, or ions causes water molecules to dissociate into atomic oxygen and hydrogen. In ref [67], it was suggested that these atoms diffuse into the silicon layers, where the oxygen reacts with silicon to form silicon-oxide (SiO_2). The introduction of oxidation-resistant capping layers (often Ru) has improved the oxidation resistance [74,75]. Another advantage of the use of a Ru capping layer is that Ru-oxidation can be reduced by atomic hydrogen [76].

Silicon oxidation and carbon deposition are primarily driven by EUV radiation and the adsorbed species and are—in that respect—not caused by the presence of EUV-induced plasma directly. Hence, these processes fall outside the scope of this review. In this distinction, other non-plasma related processes, such as heating due to EUV-irradiation, are also omitted.

An effect in EUVL that does seem to be driven by EUV-induced plasmas is blister formation on multilayer mirrors caused by delamination of the upper layers [77,78]. This delamination has been attributed to bombardment of the MLM with high energy hydrogen ions. In the following sections, the focus will be on the currently available knowledge regarding carbon removal and blister formation by EUV-induced plasmas. These plasma-surface interactions are driven by fluxes of atomic and ionic hydrogen. In this view, first, the mechanisms that determine these fluxes are discussed in Section 3.2. Finally, Section 3.3 highlights the interaction of these species with EUVL relevant surfaces.

3.2. Ionic Particle Fluxes

Particle densities and velocities towards nearby walls determine particle fluxes. Atomic hydrogen radicals have no charge and therefore plasma-induced electromagnetic fields do not influence their trajectories meaning that their flux is being determined by diffusion. Ionic species, on the other hand, are charged and are therefore accelerated by the electric fields created due to the potential difference between the bulk plasma and the surface (see previous sections). The distribution of the impact energy of these ions is determined by the electron energy distribution function (EEDF) of the EUV-induced plasma to a large extent. In EUVL, the EEDF might be significantly altered by secondary electron emission from EUV irradiated surfaces, and therefore this secondary electron emission also affects the energies and fluxes of ions towards relevant surfaces [10,21,61,79]. Metals emit electrons when they are illuminated with electromagnetic radiation with photon energies above the work function W. Of these electrons, only a small part is emitted as primary electrons straight from the surface and have energy $E_{prim} = h\upsilon - W$. However, the absorption length for EUV photons in metals is much larger than the electron mean free path in the same material. Primary electrons that are not created on the surface, but deeper in the material, undergo many scattering events before they reach the surface. This also leads to the emission of low energy (1–2 eV) secondary-electrons from the surface [80]. This effect results in a significantly lower average electron energy than one would expect solely based on the difference between the photon energy and the material's work function.

The research on the impact of secondary electron emission on EUV-induced plasma properties is limited to numerical work. Early simulations [10] on EUV-induced plasmas in 1 Pa argon show that secondary electrons lower the mean electron energy by approximately 10 eV between 50–200 ns after the EUV pulse. After 400 ns following the EUV pulse, there is no difference in charged particles density distributions, plasma potential, and average ion impact energy between simulations with and without the inclusion of secondary electrons. Recent simulations [21] in 5 Pa hydrogen yield similar observations: after 600 ns after EUV-irradiation, the influence of secondary electrons is negligible. However, the impact in the first 400 ns was larger with a 2/3 reduction in the potential when compared to the situation without the inclusion of secondary electrons. The reason for the different impact of secondary electrons on EUV-induced plasmas in argon and in hydrogen is the fact that the plasma is much denser in argon due to the larger photoionization cross section. Therefore, the relative contribution of the secondary electrons is much smaller.

Experimental work on the particle fluxes in EUV-induced plasmas has been scarce due to the limited availability of high power EUV sources. A decade ago, initial attempts to experimentally characterize the EUV-induced plasma in argon with Langmuir probes were unsuccessful [33]. The photo-electric currents that obscure the measurement of the I-V curve were the main reason for this. Later attempts showed that Langmuir probe measurements are feasible, starting from 1 μs after the EUV pulse [65,81]. Photo-electric currents still hinder probe measurements during the EUV pulse. Recently, temporally resolved retarding field energy analyzer (RFEA) measurements of ion fluxes in hydrogen plasma were published [82]. The investigated pressure range was 10–100 Pa. Similar to previous work [33], the measurements were troubled by EUV-irradiation during the first 1.5 μs. The measured ion energies peaked at bias potential, which is evidence for a collisionless space-charge region (often named the sheath region) that separates the plasma bulk from the plasma-facing surfaces. The thickness *s* of this sheath was estimated while using the Child-Langmuir law [60]. At 10 Pa, *s*

increases from 0.45 cm to 0.7 cm between 1.5 µs to 6 µs after irradiation of the gas with EUV photons. This means that the sheath needs to be considered more and more collisional, due to the increasing thickness. The same effect of increasing collisionality was found for increasing pressure.

Ion species resolved ion energy distributions towards a grounded surface have been measured while using an ion mass spectrometer [59] (See Figure 10). The flux was demonstrated to consist of H^+, H_2^+, and H_3^+ in EUV-induced plasmas in pure H_2 background gas. H_3^+ appeared to be the dominant ion due to the efficient reaction: $H_2^+ + H_2 \rightarrow H_3^+ + H$, converting the H_2^+ ion—initially produced by photo-ionization—into H_3^+. The energy distributions of H_2^+ and H_3^+ appear similar, i.e., a broad distribution with a cut-off energy at approximately 8 eV. In contrast, the IEDF of H^+ shows an energetic tail up to 18 eV. Most probably, the ions in this tail have gained energy during their creation process by dissociative photoionization and dissociative electron impact ionization [59]. Nevertheless, experimental data remains scarce and no data is available during, and shortly after, the EUV pulse, when the ion fluxes are expected to be large and ion energies to be high. The numerical models that have been extensively validated [21,81] have been able to contribute to the study of temporally resolved ion fluxes during the EUV pulse, but until now no such results have been published.
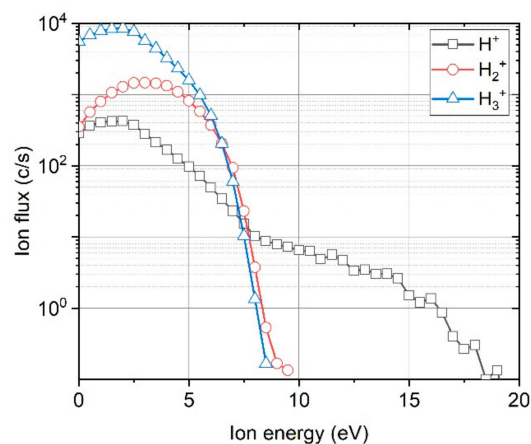
Figure 10. Time-averaged ion energy distribution functions for H^+, H_2^+, and H_3^+ ions from an EUV-induced plasma produced in H_2 gas at 5 Pa. Figure produced using data from [63].

3.3. Identification of Reaction Mechanisms

This section discusses the characterization of the mechanisms that are involved in carbon removal and multilayer delamination. The approach differs for the two phenomena, because of the different relevant time scales on which they occur.

3.3.1. Carbon Removal

The reduction of carbon layers in a hydrogen atmosphere or hydrogen plasma has been extensively studied [64,73,83–89]. The applications range from plasma processing [83–85], to cleaning in EUV related applications [64,84,87,90,91], and to nuclear fusion, where carbon is a plasma facing material candidate [85,86,88].

Carbon etching mechanisms depend on the involved particles. For example, Hydrogen atoms impact surfaces and react with the carbon surface, forming volatile hydrocarbons [73,92]. This process is especially sensitive with respect to the radical and surface temperatures [83,92]. Bombardment with hydrogen ions at moderate energies (<60 eV) results in synergetic chemical and physical etching. Initially, incident ions damage the surface, creating dangling bond sites that are available for hydrogenation. These sites can be passivated by additional ions, which leads to (volatile) hydrocarbon formation. Molecular ions below 60 eV are not dissociated when undergoing C–C bond breaking [88]. Measured sputtering yields are about 0.01 C/ion between 10–60 eV/atom [86,88].

Although the separate radicals and ions are capable of etching, the etch rate is significantly increased when both of the species are present. Combined erosion by low-energy ions and additional atomic hydrogen is described by Hopf's model [84], which has been extended for H^+ impact [86]. Again, the ions break C—C bonds, passivated by the atomic hydrogen instantaneously. This process is known as reactive ion etching.

Carbon removal by EUV-induced plasmas has been numerically and experimentally investigated [12,91] [64,91]. The carbon samples were negatively biased from 0–200 V in both of the studies. Experimentally, no etching was measured at a grounded sample in 3 Pa H_2 while using a photon fluence of 5×10^{19} cm $^{-2}$ [64]. This agrees with the experimental ion energy distributions that were measured in [59] (<8 eV) and the threshold of 10 eV. By increasing the bias voltage, and thereby the ion impact energy, yields between 0.1 C/ion and 1 C/ion were found. The difference with the ion sputtering rates that are mentioned before are attributed to the increased sputtering yields in reactive ion etching.

EUV-irradiation of the surface generates activated carbon (up to 4% of the surface carbon atoms), which is able to react with H_2 molecules, and hence increases the sputter yield. The reproducibility [91] of the experiment yielded slightly higher sputter rates, peaking at 1.9 C/ion at a −200V sample bias. No evidence was found for the increase in sputter yield due to EUV-irradiation of the surface, but the margin of error was such that it could not be excluded.

3.3.2. Multilayer Delamination

Long duration exposure tests to study multilayer optics lifetime in EUV lithography are not realistically feasible, as the lifetime target is 30,000 h [93]. Therefore, adequately predicting delamination requires a thorough understanding of the interaction mechanisms between EUV-induced plasmas and those surfaces exposed. Thus far, delamination studies have been focusing on ion-surface interactions where ion fluxes were generated while using alternative sources, like thermal gas crackers [94,95] or an ion gun [96].

Delamination in Mo/Si multilayer samples due to ion irradiation has been experimentally confirmed using moderate energy (50–200 eV) [96,97] and energetic (>800 eV) hydrogen ions [95,98]. E.g., deuterium ions have been shown to be capable of having an eroding effect on both Mo and Si layer of EUV lithography relevant optical materials [94]. Multilayer delamination has been shown, even under low ion flux conditions, if the exposure time and thus the total ion fluence was sufficient [99]. Some of these studies [77,94–96,99] relate their work to mirror degradation in EUV lithography by suggesting that the used ion sources serve as a proxy for the ion fluxes that are created by an EUV-induced plasma. This approach is valid for the first few microseconds after the EUV pulse, in a collisionless regime and while using biased surfaces [82]. However, this approach is not fully valid for longer time scales due to the increasing sheath thickness and the resulting transit to a collisional regime. Increased pressures (i.e., up to 100 Pa) appear to have the same effect. Furthermore, the IEDF towards grounded or floating walls consists of large fractions of low energy (<10 eV) ions [59]. Therefore, the validity of the used ion sources as a proxy for EUV-induced plasmas strongly depends on the targeted experimental conditions. For now, the investigation of the influence of ion fluxes on EUV lithography relevant optics materials has been limited to equivalence studies for collisionless sheath conditions the near biased surfaces.

4. Discussion, Conclusions, and Outlook

EUV-induced plasma is a highly-transient and peculiar type of plasma with significant impact on EUVL equipment and processes, as may have become clear from this contribution. Although numerical and experimental research campaigns have enlightened several of this plasma's secrets, several aspects of it remain unexplored. Below, we define some of the most urgent research areas as being interesting from both a fundamental and EUVL application point of view. Note that new research project in some of these directions have already been recently initiated by the authors.

- Radical production

With regards to bulk plasma and from an experimental point of view, electrons and ions have already been characterized. However, in the full picture the characterization of radicals (e.g., atomic H) is lacking, despite their potential impact on cleaning and lifetime issues. More knowledge with respect to radical production could be gained through plasma-chemical (numerical) models and experiments utilizing techniques, such as UV absorption or Two-photon Absorption Laser Induced Fluorescence (TALIF).

- Gas admixtures (e.g., N_2)

Up to now, most of the studies have only been performed in hydrogen (or argon only or helium only). However, the addition of small amounts of other gases can have an important influence on the composition of the EUV-induced plasma and it might significantly alter plasma chemistry and plasma physical processes, and hence representing real scanner conditions more accurately [62]. Although the first explorative study on N_2-dilution of EUV-induced plasmas in H_2 has recently been published [63], there remains a strong demand from industry to understand the effect of other gases/vapors (e.g., H_2O, O_2, and N_2) on the whole model of EUV-induced plasma dynamics.

- Interaction with nano- to micrometer sized particles

Although EUV-induced plasma dynamics and the impact thereof are much better understood than 10 years ago, the interaction of nano- to micrometer sized particles with the complex atmosphere of an EUV lithography tool (including plasma, electric fields, energetic photons, etc.) is a blank spot that should be enlightened. The reason for the importance of plasma-particle interaction is the fact that bulk plasma normally has higher potential when compared to its surroundings [60]. This, in combination with the ability of plasma to deliver high surface charges to the particles [100], gives rise to concerns regarding particle transport from the location where the particles are released to basically every other location in the tool where the particles may harm. Whereas, in normal low pressure plasmas, the charge on micrometer-sized particles is permanently negative and it ranges in magnitude from a few 1000 times the elementary charge in the space charge regions at the plasma's border [48,101,102] up to a few 10^5 times the elementary charge in the plasma bulk [100], the charge on particles under EUVL tool conditions may significantly vary and may even become positive for certain fractions of the time. It is especially the transient behavior of the kind of plasmas occurring in EUVL tools and the presence of ionizing radiation that can have considerable influence on the dynamic particle charging from both a temporal [103] and a spatial [104] point of view. We expect in the coming decade enhanced research efforts in the field of Complex Ionized Media (CIM) with nano-contamination control becoming more dominantly important for EUVL and with (EUV-induced) plasma being a strong candidate with respect to achieving cleanliness targets, i.e., the field studying the interaction between nano-contaminants and ionized media.

With respect to the interaction of EUV-induced plasma with plasma-facing materials, in general, the understanding does not extend much beyond what is known from classic (discharge) plasma physics. Processes that affect the evolution of space charge regions and the formation of a sheath are theorized, but the limited available experimental work cannot support all of the claims made. Especially, the first 100 ns to 1 μs of the ion flux evolution (after the gas is irradiated with a pulsed beam of EUV photons) have not been experimentally explored. This troubles predictions regarding the lifetime of optical components, because full duration lifetime tests are not feasible. Beyond these issues that have been under investigation, scaling laws for EUV-induced plasma material interaction with respect to applied pulse energy, repetition rate, and gas pressure/type are not explored yet. Especially, the buildup of a steady state background plasma at high repetition rates may significantly impact the ion fluence towards walls.

Conflicts of Interest: The authors declare no conflict of interest.

References

1. Born, M.; Wolf, E. *Principles of Optics*; Pegamon Press: Oxford, UK, 1980.
2. Lin, B.J. The future of subhalf-micrometer optical lithography. *Microelectron. Eng.* **1987**, *6*, 31–51. [CrossRef]
3. *EUV Lithography*, 2nd ed.; Bakshi, V. (Ed.) SPIE Press: Bellingham, WA, USA, 2018.
4. Benschop, J.; Banine, V.; Lok, S.; Loopstra, E. Extreme ultraviolet lithography: Status and prospects. *J. Vac. Sci. Technol. B* **2008**, *26*, 2204–2207. [CrossRef]
5. Bergmann, K.; Schriever, G.; Rosier, O.; Müller, M.; Neff, W.; Lebert, R. Highly repetitive, extreme-ultraviolet radiation source based on a gas-discharge plasma. *Appl. Opt.* **1999**, *38*, 5413–5417. [CrossRef] [PubMed]
6. Fomenkov, I.V.; Brandt, D.C.; Farrar, N.R.; La Fontaine, B.; Böwering, N.R.; Brown, D.J.; Ershov, A.I.; Myers, D.W. Laser Produced Plasma EUV Light Source for EUVL Patterning at 20nm Node and Beyond. *Extreme Ultrav. (EUV) Lithogr. IV* **2013**, *8679*, 86792I.
7. Brandt, D.C.; Fomenkov, I.V.; Farrar, N.R.; La Fontaine, B.; Myers, D.W.; Brown, D.J.; Ershov, A.I.; Böwering, N.R.; Riggs, D.J.; Rafac, R.J.; et al. LPP EUV source readiness for NXE 3300B. *Extreme Ultrav. (EUV) Lithogr. V* **2014**, *9048*, 90480C.
8. Ueno, Y.; Hori, T.; Kawasuji, Y.; Shiraishi, Y.; Yanagida, T.; Miyao, K.; Hayashi, H.; Ishii, T.; Watanabe, Y.; Okamoto, T.; et al. Key Components Development Progress Updates of the 250W High Power LPP-EUV Light Source. *Extreme Ultrav. (EUV) Lithogr. IX* **2018**, *10583*, 1058328.
9. Teramoto, Y.; Santos, B.; Mertens, G.; Kops, R.; Kops, M.; von Wezyk, A.; Bergmann, K.; Yabuta, H.; Nagano, A.; Ashizawa, N.; et al. High-radiance LDP source for mask inspection and beam line applications (Conference Presentation). *Extreme Ultrav. (EUV) Lithogr. VIII* **2017**, *10143*, 101431L.
10. Van der Velden, M.H.L.; Brok, W.J.M.; Van der Mullen, J.J.A.M.; Banine, V. Kinetic simulation of an extreme ultraviolet radiation driven plasma near a multilayer mirror. *J. Appl. Phys.* **2006**, *100*, 73303. [CrossRef]
11. Van Der Horst, R.M.; Beckers, J.; Osorio, E.A.; Banine, V.Y. Exploring the electron density in plasmas induced by extreme ultraviolet radiation in argon. *J. Phys. D Appl. Phys.* **2015**, *48*, 285203. [CrossRef]
12. Astakhov, D. *Numerical Study of Extreme-Ultra-Violet Generated Plasmas in Hydrogen*; Universiteit Twente: Enschede, The Netherlands, 2016.
13. Yoon, J.S.; Song, M.Y.; Han, J.M.; Hwang, S.H.; Chang, W.S.; Lee, B.; Itikawa, Y. Cross Sections for Electron Collisions with Hydrogen Molecules. *J. Phys. Chem. Ref. Data* **2008**, *37*, 913–931. [CrossRef]
14. Ehrhardt, H.; Langhans, L.; Linder, F.; Taylor, H.S. Resonance scattering of slow electrons from H 2 and CO angular distributions. *Phys. Rev.* **1968**, *173*, 222–230. [CrossRef]
15. Bakshi, V. *EUV Sources for Lithography*; Bakshi, V., Ed.; Spie Press: Bellingham, WA, USA, 2006.
16. Van der Horst, R.M. *Electron Dynamics in EUV-Induced Plasmas*; Eindhoven University of Technology: Eindhoven, The Netherlands, 2015.
17. Van Der Horst, R.M.; Beckers, J.; Osorio, E.A.; Astakhov, D.I.; Goedheer, W.J.; Lee, C.J.; Ivanov, V.V.; Krivtsum, V.M.; Koshelev, K.N.; Lopaev, D.V.; et al. Exploring the electron density in plasma induced by EUV radiation: I. Experimental study in hydrogen. *J. Phys. D Appl. Phys.* **2016**, *19*, 145203. [CrossRef]
18. Beckers, J.; van Der Horst, R.M.; Osorio, E.A.; Kroesen, G.M.W.; Banine, V.Y. Thermalization of electrons in decaying extreme ultraviolet photons induced low pressure argon plasma. *Plasma Source Sci. Technol.* **2016**, *15*, 35010. [CrossRef]
19. Birdsall, A.; Langdon, C. *Plasma Physics via Computer Simulation*; CRC Press: Boca Raton, FL, USA, 1991.
20. Wieggers, R.C.; Goedheer, W.J.; Louis, E.; Bijkerk, F. Plasma-induced damage of multilayer coatings in EUVL. *Proc. SPIE 6586 Damage VUV EUV X-ray Opt.* **2007**, *6586*, 65860L.
21. Astakhov, D.I.; Goedheer, W.J.; Lee, C.J.; Ivanov, V.V.; Krivtsun, V.M.; Koshelev, K.N.; Lopaev, D.V.; Van Der Horst, R.M.; Beckers, J.; Osorio, E.A.; et al. Exploring the electron density in plasma induced by EUV radiation: II. Numerical studies in argon and hydrogen. *J. Phys. D Appl. Phys.* **2016**, *49*, 295204. [CrossRef]
22. Astakhov, D.I.; Goedheer, W.J.; Lee, C.J.; Ivanov, V.V.; Krivtsun, V.M.; Zotovich, A.I.; Zyryanov, S.M.; Lopaev, D.V.; Bijkerk, F. Plasma probe characteristics in low density hydrogen pulsed plasmas. *Plasma Source Sci. Technol.* **2015**, *24*, 55018. [CrossRef]
23. Mokrov, M.S.; Raizer, Y.P. Monte Carlo method for finding the ionization and secondary emission coefficients and I–V characteristic of a Townsend discharge in hydrogen. *Tech. Phys.* **2008**, *53*, 436–444. [CrossRef]
24. Van de Ven, T.H.M. *Ion Fluxes Towards Surfaces Exposed to EUV-Induced Plasmas*; Eindhoven University of Technology: Eindhoven, The Netherlands, 2018.

25. Hobbs, G.D.; Wesson, J.A. Heat flow through a Langmuir sheath in the presence of electron emission. *Plasma Phys.* **1967**, *9*, 85. [CrossRef]

26. Van der Horst, R.M.; Beckers, J.; Osorio, E.A.; van de Ven, T.H.M.; Banine, V.Y. Radiating plasma species density distribution in EUV-induced plasma in argon: A spatiotemporal experimental study. *Plasma Source Sci. Technol.* **2015**, *24*, 065016. [CrossRef]

27. Bartnik, A.; Skrzeczanowski, W.; Wachulak, P.; Saber, I.; Fiedorowicz, H.; Fok, T. Low-temperature photoionized plasmas induced in Xe gas using an EUV source driven by nanosecond laser pulses. *Laser Part. Beams* **2017**, *35*, 42–47. [CrossRef]

28. Bartnik, A.; Fiedorowicz, H.; Wachulak, P.; Fok, T. Time-resolved measurements of extreme ultraviolet (EUV) emission, from EUV-induced He, Ne, and Ar plasmas. *Laser Part. Beams* **2019**, *37*, 49–54. [CrossRef]

29. Bartnik, A.; Wachulak, P.; Fiedorowicz, H.; Fok, T.; Jarocki, R.; Szczurek, M. Extreme ultraviolet-induced photoionized plasmas. *Phys. Scr.* **2014**, *T161*, 14061. [CrossRef]

30. Bartnik, A.; Wachulak, P.; Fok, T.; Fiedorowicz, H.; Skrzeczanowski, W.; Pisarczyk, T.; Chodukowski, T.; Kalinowska, Z.; Dudzak, R.; Dostal, J.; et al. Photoionized argon plasmas induced with intense soft x-ray and extreme ultraviolet pulses. *Plasma Phys. Control. Fusion* **2015**, *58*, 14009. [CrossRef]

31. Saber, I.; Bartnik, A.; Wachulak, P.; Skrzeczanowski, W.; Jarocki, R.; Fiedorowicz, H. Temporal variations of electron density and temperature in Kr/Ne/H2 photoionized plasma induced by nanosecond pulses from extreme ultraviolet source. *Phys. Plasmas* **2017**, *24*, 063501. [CrossRef]

32. Carbone, E.; Nijdam, S. Thomson scattering on non-equilibrium low density plasmas: Principles, practice and challenges. *Plasma Phys. Control. Fusion* **2015**, *57*, 014026. [CrossRef]

33. Van der Velden, M. *Radiation Generated Plasmas: A Challenge in Modern Lithography*; University of Technology Eindhoven: Eindhoven, The Netherlands, 2008.

34. Van der Horst, R.M.; Beckers, J.; Nijdam, S.; Kroesen, G.M.W. Exploring the temporally resolved electron density evolution in extreme ultra-violet induced plasmas. *J. Phys. D Appl. Phys.* **2014**, *47*, 302001. [CrossRef]

35. Van der Horst, R.M.; Osorio, E.A.; Banine, V.Y.; Beckers, J. The influence of the EUV spectrum on plasma induced by EUV radiation in argon and hydrogen gas. *Plasma Source Sci. Technol.* **2016**, *25*, 015012. [CrossRef]

36. De Wetering, F. Dust Particle Formation in Silane Plasmas. Ph.D. Thesis, Eindhoven University of Technology, Eindhoven, The Netherlands, 2005.

37. Brown, S.C.; Rose, D.J. Methods of measuring the properties of ionized gases at high frequencies. I. Measurements of Q. *J. Appl. Phys.* **1952**, *23*, 711–718. [CrossRef]

38. Rose, D.J.; Brown, S.C. Methods of measuring the properties of ionized gases at high frequencies. II. Measurement of electric field. *J. Appl. Phys.* **1952**, *23*, 719–722. [CrossRef]

39. Rose, D.J.; Brown, S.C. Methods of measuring the properties of ionized gases at high frequencies. III. Measurement of discharge admittance and electron density. *J. Appl. Phys.* **1952**, *23*, 1028–1032. [CrossRef]

40. Haverlag, M.; Kroesen, G.M.W.; Bisschops, T.H.J.; DeHoog, F.J. Measurement of electron-densities by a microwave cavity method 13.56-MHz RF plasmas of AR, CF4, C2F6, and CHF3. *Plasma Chem. Plasma Process.* **1991**, *11*, 357–370. [CrossRef]

41. Stoffels, E.; Stoffels, W.W.; Vender, D.; Kando, M.; Kroesen, G.M.W.; DeHoog, F.J. Negative ions in a radiofrequency oxygen plasmas. *Phys. Rev. E* **1995**, *51*, 2425–2435. [CrossRef]

42. Stoffels, E.; Stoffels, W.W. Electrons, Ions and Dust in a Radio-Frequency Discharge. Ph.D. Thesis, Eindhoven University of Technology, Eindhoven, The Netherlands, 1994.

43. Vender, D.; Stoffels, W.W.; Stoffels, E.; Kroesen, G.M.W.; DeHoog, F.J. Charged-species profiles in electronegative radiofrequency plasmas. *Phys. Rev. E* **1995**, *51*, 2436–2444. [CrossRef]

44. Stoffels, W.W.; Sorokin, M.; Remy, J. Charge and charging of nanoparticles in a SiH4 rf-plasma. *Faraday Discuss.* **2008**, *137*, 115–126. [CrossRef] [PubMed]

45. Van de Wetering, F.M.J.H.; Beckers, J.; Kroesen, G.M.W. Anion dynamics in the first 10 milliseconds of an argon-acetylene radio-frequency plasma. *J. Phys. D Appl. Phys.* **2012**, *45*, 485205. [CrossRef]

46. Van de Wetering, F.M.J.H.; Brooimans, R.J.C.; Nijdam, S.; Beckers, J.; Kroesen, G.M.W. Fast and interrupted expansion in cyclic void growth in dusty plasma. *J. Phys. D Appl. Phys.* **2015**, *48*, 035204. [CrossRef]

47. Beckers, J.; Stoffels, W.W.; Kroesen, G.M.W. Temperature dependence of nucleation and growth of nanoparticles in low pressure Ar/CH4 RF discharges. *J. Phys. D Appl. Phys.* **2009**, *42*, 155206. [CrossRef]

48. Beckers, J. Dust Particle(s) (as) Diagnostics in Plasmas. Ph.D. Thesis, Eindhoven University of Technology, Eindhoven, The Netherlands, 2011.

49. Van der Schans, M.; Platier, B.; Koelman, P.; van de Wetering, F.; van Dijk, J.; Beckers, J.; Nijdam, S.; IJzerman, W. Decay of the electron density and the electron collision frequency between successive discharges of a pulsed plasma jet in N2. *Plasma Source Sci. Technol.* **2019**, *28*, 35020. [CrossRef]

50. Van der Horst, R.M.; Beckers, J.; Osorio, E.A.; Banine, V.Y. Dynamics of the spatial electron density distribution of EUV-induced plasmas. *J. Phys. D Appl. Phys.* **2015**, *48*, 432001. [CrossRef]

51. Beckers, J.; Van De Wetering, F.M.J.H.; Platier, B.; Van Ninhuijs, M.A.W.; Brussaard, G.J.H.; Banine, V.Y.; Luiten, O.J. Mapping electron dynamics in highly transient {EUV} photon-induced plasmas: A novel diagnostic approach using multi-mode microwave cavity resonance spectroscopy. *J. Phys. D Appl. Phys.* **2018**, *52*, 34004. [CrossRef]

52. Banine, V.Y. Radiation sensor apparatus. US-20180058928-A1 1 March 2018.

53. Chung, Y.M.; Lee, E.M.; Masuoka, T.; Samson, J.A.R. Dissociative Photoionization Of H2 From 18 To 124-Ev. *J. Chem. Phys.* **1993**, *99*, 885–889. [CrossRef]

54. Kossmann, H.; Schwarzkopf, O.; Kammerling, B.; Braun, W.; Schmidt, V. Photoionisation cross-section of h-2. *J. Phys. B Atomic Mol. Opt. Phys.* **1989**, *22*, L411–L414. [CrossRef]

55. Dujardin, G.; Besnard, M.J.; Hellner, L.; Malinovitch, Y. Double photoionization of H_2: An experimental test of electronic-correlation models in molecules. *Phys. Rev. A* **1987**, *35*, 5012–5019. [CrossRef]

56. Berkowiz, J. Atomic and Molecular Photoabsorption: Absolute Partial Cross Sections. Elsevier Science Academic Press: Cambridge, MA, USA, 2015.

57. McCulloh, K.E.; Rosenstock, H.M. Experimental Test of the Franck—Condon Principle: Double Ionization of Molecular Hydrogen. *J. Chem. Phys.* **1968**, *48*, 2084–2089. [CrossRef]

58. Tabata, T.; Shirai, T. Analytic Cross Sections For Collisions Of H+, H2+, H3+, H, H2, And H− With Hydrogen Molecules. *At. Data Nucl. Data Tables* **2000**, *76*, 1–25. [CrossRef]

59. Van De Ven, T.H.M.; Reefman, P.; De Meijere, C.A.; Van Der Horst, R.M.; Van Kampen, M.; Banine, V.Y.; Beckers, J. Ion energy distributions in highly transient EUV induced plasma in hydrogen. *J. Appl. Phys.* **2018**, *123*, 063301. [CrossRef]

60. Lieberman, M.A.; Lichtenberg, A.J. *Principles of Plasma Discharges and Materials Processing*, 2nd ed.; John Wiley & Sons, Inc.: Hoboken, NJ, USA, 2005.

61. Van der Velden, M.; Brok, W.; van der Mullen, J.; Goedheer, W.; Banine, V. Particle-in-cell Monte Carlo simulations of an extreme ultraviolet radiation driven plasma. *Phys. Rev. E* **2006**, *73*, 36406. [CrossRef]

62. Samson, J.A.; Masuoka, T.; Pareek, P.N.; Angel, G.C. Total and dissociative photoionization cross sections of N2 from threshold to 107 eV. *J. Chem. Phys.* **1987**, *86*, 6128. [CrossRef]

63. Beckers, J.; de Ven, T.H.M.; de Meijere, C.A.; der Horst, R.M.; van Kampen, M.; Banine, V.Y. Energy distribution functions for ions from pulsed EUV-induced plasmas in low pressure N_2-diluted H_2 gas. *Appl. Phys. Lett.* **2019**, *114*, 133502. [CrossRef]

64. Dolgov, A.; Lopaev, D.; Rachimova, T.; Kovalev, A.; Vasil'Eva, A.; Lee, C.J.; Krivtsun, V.M.; Yakushev, O.; Bijkerk, F. Comparison of H_2 and He carbon cleaning mechanisms in extreme ultraviolet induced and surface wave discharge plasmas. *J. Phys. D Appl. Phys.* **2014**, *47*, 65205. [CrossRef]

65. Dolgov, A.; Lopaev, D.; Lee, C.J.; Zoethout, E.; Medvedev, V.; Yakushev, O.; Bijkerk, F. Characterization of carbon contamination under ion and hot atom bombardment in a tin-plasma extreme ultraviolet light source. *Appl. Surf. Sci.* **2015**, *353*, 708–713. [CrossRef]

66. Boller, K.; Haelbich, R.P.; Hogrefe, H.; Jark, W.; Kunz, C. Investigation of carbon contamination of mirror surfaces exposed to synchrotron radiation. *Nucl. Instrum. Methods Phys. Res.* **1983**, *208*, 273–279. [CrossRef]

67. Koster, N.; Mertens, B.; Jansen, R.; Van De Runstraat, A.; Stietz, F.; Wedowski, M.; Meiling, H.; Klein, R.; Gottwald, A.; Scholze, F.; et al. Molecular contamination mitigation in EUVL by environmental control. *Microelectron. Eng.* **2002**, *61*, 65–76. [CrossRef]

68. Malinowski, M.E.; Steinhaus, C.; Clift, W.M.; Klebanoff, L.E.; Mrowka, S. Controlling contamination in Mo/Si multilayer mirrors by Si surface capping modifications. *Proc. SPIE* **2002**, *4688*, 442–453.

69. Meiling, H.; Meijer, H.; Banine, V.; Moors, R.; Groeneveld, R.; Voorma, H.J.; Mickan, U.; Wolschrijn, B.; Mertens, B.; van Baars, G.; et al. First performance results of the ASML alpha demo tool. *Proc. SPIE* **2006**, *6151*, 615108.

70. Matsunari, S.; Aoki, T.; Murakami, K.; Gomei, Y.; Terashima, S.; Takase, H.; Tanabe, M.; Watanabe, Y.; Kakutani, Y.; Niibe, M.; et al. Carbon deposition on multi-layer mirrors by extreme ultra violet ray irradiation. *Proc. SPIE Int. Soc. Opt. Eng.* **2007**, *6517*, 65172X.

71. Hollenshead, J.; Klebanoff, L. Modeling radiation-induced carbon contamination of extreme ultraviolet optics. *J. Vac. Sci. Technol. B Microelectron. Nanom. Struct.* **2006**, *24*, 64. [CrossRef]

72. Koster, N.B.; van der Donck, J.C.J.; Stortelder, J.K.; de Jong, A.J.; Molkenboer, F.T. A multistep approach for reticle cleaning. *Proc. SPIE* **2012**, *8322*, 83220R.

73. Chen, J.; Louis, E.; Harmsen, R.; Tsarfati, T.; Wormeester, H.; van Kampen, M.; van Schaik, W.; van de Kruijs, R.; Bijkerk, F. In situ ellipsometry study of atomic hydrogen etching of extreme ultraviolet induced carbon layers. *Appl. Surf. Sci.* **2011**, *258*, 7–12. [CrossRef]

74. Bajt, S.; Alameda, J.B.; Clift, W.M.; Folta, J.A.; Kaufmann, B.; Spiller, E.A. Improved reflectance and stability of Mo-Si multilayers. *Opt. Eng.* **2002**, *41*, 1797. [CrossRef]

75. Yakshinskiy, B.V.; Bartynski, R.A. Carbon film growth on model MLM cap layer: Interaction of selected hydrocarbon vapor with Ru(10(1)over-bar0) surface. *Extreme Ultrav. (Euv) Lithogr.* **2010**, *7636*, 76360F.

76. Oizumi, H.; Izumi, A.; Motai, K.; Nishiyama, I.; Namiki, A. Atomic hydrogen cleaning of surface Ru oxide formed by extreme ultraviolet irradiation of Ru-capped multilayer mirrors in H2O ambience. *Jpn. J. Appl. Phys.* **2007**, *46*, L633. [CrossRef]

77. Bondareva, A.L.; Zmievskaya, G.I. Computer simulation of blistering in multilayer mirrors for EUV lithography. *J. Surf. Investig. X-ray, Synchrotron Neutron Tech.* **2010**, *4*, 480–487. [CrossRef]

78. Enhanced multilayer mirror stability through heterogeneous materials. Available online: https://www.rvo.nl/subsidies-regelingen/projecten/enhanced-multilayer-mirror-stability-through-heterogeneous-materials (accessed on 13 July 2019).

79. Wieggers, R.C.; Goedheer, W.J.; Akdim, M.R.; Bijkerk, F.; Zegeling, P.A. A particle-in-cell plus Monte Carlo study of plasma-induced damage of normal incidence collector optics used in extreme ultraviolet lithography. *J. Appl. Phys.* **2008**, *3*, 013308. [CrossRef]

80. Henke, B.L.; Gullikson, E.M.; Davis, J.C. X-Ray Interactions: Photoabsorption, Scattering, Transmission, and Reflection at E = 50-30,000 eV, Z = 1-92. *At. Data Nucl. Data Tables* **1993**, *54*, 181–342. [CrossRef]

81. Abrikosov, A.; Reshetnyak, V.; Astakhov, D.; Dolgov, A.; Yakushev, O.; Lopaev, D.; Krivtsun, V. Numerical simulations based on probe measurements in EUV-induced hydrogen plasma. *Plasma Source Sci. Technol.* **2017**, *26*, 45011. [CrossRef]

82. Abrikosov, A.A.; Yakushev, O.F.; Lopaev, D.V.; Krivtsun, V.M. Dynamics of the ion energy spectrum in EUV-induced hydrogen plasma. *Plasma Phys. Rep.* **2017**, *43*, 614–620. [CrossRef]

83. Jariwala, B.N.; Ciobanu, C.V.; Agarwal, S. Atomic hydrogen interactions with amorphous carbon thin films. *J. Appl. Phys.* **2009**, *106*, 073305. [CrossRef]

84. Hopf, C.; von Keudell, A.; Jacob, W. Chemical sputtering of hydrocarbon films. *J. Appl. Phys.* **2003**, *94*, 2373–2380. [CrossRef]

85. Schlüter, M.; Hopf, C.; Jacob, W. Chemical sputtering of carbon by combined exposure to nitrogen ions and atomic hydrogen. *New J. Phys.* **2008**, *10*, 53037. [CrossRef]

86. Liu, S.; Sun, J.; Dai, S.; Stirner, T.; Wang, D. A general model for chemical erosion of carbon materials due to low-energy H+ impact. *J. Appl. Phys.* **2010**, *108*, 073302. [CrossRef]

87. Nishiyama, Y.; Anazawa, T.; Oizumi, H.; Nishiyama, I.; Suga, O.; Abe, K.; Kagata, S.; Izumi, A. Carbon contamination of EUV mask: Film characterization, impact on lithographic performance, and cleaning. *Emerg. Lithogr. Technol. XII PTS 1 2* **2008**, *6921*, 692116.

88. Meyer, F.W.; Zhang, H.; Lance, M.J.; Krause, H.F. Chemical sputtering and surface damage of graphite by low-energy atomic and molecular hydrogen and deuterium projectiles. *Vacuum* **2008**, *82*, 880–887. [CrossRef]

89. Elg, D.T.; Panici, G.A.; Srivastava, S.N.; Ruzic, D.N. Collector Optic Cleaning by In-Situ Hydrogen Plasma. *Extreme Ultrav. (EUV) Lithogr. VI* **2015**, *9422*, 94222H.

90. Chen, J.; Louis, E.; Wormeester, H.; Harmsen, R.; van de Kruijs, R.; Lee, C.J.; van Schaik, W.; Bijkerk, F. Carbon-induced extreme ultraviolet reflectance loss characterized using visible-light ellipsometry. *Meas. Sci. Technol.* **2011**, *22*, 105705. [CrossRef]

91. Astakhov, D.I.; Goedheer, W.J.; Lee, C.J.; Ivanov, V.V.; Krivtsun, V.M.; Yakushev, O.; Koshelev, K.N.; Lopaev, D.V.; Bijkerk, F. Numerical and experimental studies of the carbon etching in EUV-induced plasma. *arXiv* **2016**, arXiv:1507.02705.

92. Biener, J.; Schenk, A.; Winter, B.; Lutterloh, C.; Horn, A.; Kuppers, J. Elementary Steps Of The Interaction Of C-H Film Surfaces With Thermal H/D Atoms. *Vacuum* **1995**, *46*, 903–906. [CrossRef]

93. Meiling, H.; Banine, V.; Kurz, P.; Blum, B.; Heerens, G.J.; Harned, N. The EUV program at ASML: An update. *Emerg. Lithogr. Technol. VII Pts 1 2* **2003**, *5037*, 24–35.

94. Kuznetsov, A.S.; Kruijs, R.W.E.; Gleeson, M.A.; Schmid, K.; Bijkerk, F. Hydrogen interaction with EUVL-relevant optical materials. *J. Surf. Investig. X-ray, Synchrotron Neutron Tech.* **2010**, *4*, 563–566. [CrossRef]

95. Kuznetsov, A.S.; Gleeson, M.A.; Bijkerk, F. Ion effects in hydrogen-induced blistering of Mo/Si multilayers. *J. Appl. Phys.* **2013**, *114*, 113507. [CrossRef]

96. Van den Bos, R.A.J.M.; Lee, C.J.; Benschop, J.P.H.; Bijkerk, F. Blister formation in Mo/Si multilayered structures induced by hydrogen ions. *J. Phys. D Appl. Phys.* **2017**, *50*, 265302. [CrossRef]

97. Van den Bos, R.A.J.M.; Reshetniak, V.; Lee, C.J.; Benschop, J.; Bijkerk, F. A model for pressurized hydrogen induced thin film blisters. *J. Appl. Phys.* **2016**, *120*, 235304. [CrossRef]

98. Pelizzo, M.G.; Corso, A.J.; Zuppella, P.; Windt, D.L.; Mattei, G. Stability of extreme ultraviolet multilayer coatings to low energy proton bombardment. *Opt. Express* **2011**, *19*, 14838–14844. [CrossRef]

99. Kuznetsov, A.S.; Gleeson, M.A.; van de Kruijs, R.W.E.; Bijkerk, F. Blistering behavior in Mo/Si multilayers. *Damage VUV, EUV X-ray Optics III* **2011**, *8077*, 807713.

100. Bouchoule, A. *Dusty Plamsas; Physics, Chemistry and Technological Impacts in Plasma Processing*; John Wiley And Sons Ltd.: Chichester, UK, 1999.

101. Beckers, J.; Ockenga, T.; Wolter, M.; Stoffels, W.W.; Van Dijk, J.; Kersten, H.; Kroesen, G.M.W. Microparticles in a collisional rf plasma sheath under hypergravity conditions as probes for the electric field strength and the particle charge. *Phys. Rev. Lett.* **2011**, *106*, 115002. [CrossRef] [PubMed]

102. Beckers, J.; Trienekens, D.J.M.; Kroesen, G.M.W. Absolute measurement of the total ion-drag force on a single plasma-confined microparticle at the void edge under microgravity conditions. *Phys. Rev. E Stat. Nonlinear Soft Matter Phys.* **2013**, *88*, 055101. [CrossRef] [PubMed]

103. Ivlev, A.V.; Kretschmer, M.; Zuzic, M.; Morfill, G.E.; Rothermel, H.; Thomas, H.M.; Fortov, V.E.; Molotkov, V.I.; Nefedov, A.P.; Lipaev, A.M.; et al. Decharging of complex plasmas: First kinetic observations. *Phys. Rev. Lett.* **2003**, *90*, 055003/1–055003/4. [CrossRef] [PubMed]

104. Van Minderhout, B.; Peijnenburg, T.; Blom, P.; Vogels, J.M.; Kroesen, G.M.; Beckers, J. The charge of micro-particles in a low pressure spatial plasma afterglow. *J. Phys. D Appl. Phys.* **2019**, *52*, 32. [CrossRef]